



# Hot Corrosion Behavior of Ni20Cr Alloy in NaVO<sub>3</sub> Molten Salt

P.D. Silva-Leon, O. Sotelo-Mazon, G. Salinas-Solano, J. Porcayo-Calderon, J.G. Gonzalez-Rodriguez, S. Valdez, and L. Martinez-Gomez

(Submitted September 8, 2018; in revised form July 7, 2019; published online July 29, 2019)

The hot corrosion behavior of Ni20Cr alloy was evaluated in NaVO<sub>3</sub> at temperatures of up to 700 °C and compared to Inconel 600. The performance of both the alloys was evaluated using electrochemical measurements, such as potentiodynamic polarization, linear polarization resistance, and electrochemical impedance spectroscopy measurements, as well as a cyclic corrosion test. The results show that the Ni20Cr alloy has better corrosion performance than the Inconel 600. The better performance of the Ni20Cr alloy was due to its ability to develop a stable protector oxide (Cr<sub>2</sub>O<sub>3</sub>) on its surface.

**Keywords** cyclic corrosion, electrochemical techniques, hot corrosion, Ni20Cr alloy, oxide

## 1. Introduction

High-temperature corrosion is a serious issue in power generation systems and is influenced by the type of fuel, fuel conditions, and design factors of the system (Ref 1). Low-grade fuels, also known as residual fuels, are commonly used in power generation systems due to the high cost of high-grade fuels. However, low-grade fuels contain high concentrations of vanadium, sulfur, and sodium impurities. These elements are harmful because they form highly corrosive compounds during the fuel oil combustion, such as V<sub>2</sub>O<sub>5</sub>, V<sub>2</sub>O<sub>4</sub>, Na<sub>2</sub>SO<sub>4</sub>, NaVO<sub>3</sub>, and vanadate complexes. These compounds are deposited by condensation as thin films of molten salts on the surfaces of materials.

One of the most probable reactions takes place between vanadium oxide (V<sub>2</sub>O<sub>5</sub>) and sodium sulfate (Na<sub>2</sub>SO<sub>4</sub>), which forms sodium vanadate (NaVO<sub>3</sub>, Na<sub>4</sub>V<sub>2</sub>O<sub>7</sub>, Na<sub>3</sub>VO<sub>4</sub>) and vanadate complexes. These compounds are among the most corrosive due to their low melting points, low viscosity, and acidity, which lead to accelerated dissolution of the protective oxide layer that develops on the surfaces of metallic materials. This accelerated attack is known as hot corrosion (Ref 2-7). Some ways to prevent corrosive attacks of molten salts are replacing conventional materials (stainless steel) with more

resistant alloys, such as Ni- or Co-based superalloys, using metallic coatings that form a stable film of protective oxides, such as Cr<sub>2</sub>O<sub>3</sub>, Al<sub>2</sub>O<sub>3</sub>, and SiO<sub>2</sub>; and using inhibitors (CaO and MgO) that can form vanadates with high melting points (Mg<sub>3</sub>V<sub>2</sub>O<sub>8</sub>, Mg<sub>2</sub>V<sub>2</sub>O<sub>7</sub>) (Ref 5, 7).

Superalloys are more commonly used in high-temperature industrial process because they have good mechanical properties, such as tensile resistance, creep, and fatigue resistance, and they maintain microstructural stability over a wide range of temperatures (Ref 7). The high-temperature corrosion resistance of superalloys is based on their ability to develop stable protective oxide films on their surfaces, such as Cr<sub>2</sub>O<sub>3</sub> or Al<sub>2</sub>O<sub>3</sub>, which is due to the selective oxidation of protective elements. Generally, Ni-based superalloys are the most popular due to their high content of Cr, which provides excellent corrosion resistance. This is due to the development of a protective oxide (Cr<sub>2</sub>O<sub>3</sub>), which decreases the aggressive effects of the corrosive species present in vanadium or sulfate salts (Ref 2, 8, 9). The formation of a continuous protective layer of Cr<sub>2</sub>O<sub>3</sub> is possible as long as the chromium content of the alloy is at least 10-15% by weight (Ref 10). Although the formation of a protective layer of Cr<sub>2</sub>O<sub>3</sub> increases the corrosion resistance of the superalloys, it has been reported that the continuous dissolution of the protective layer promotes the formation of various oxides due to the different elements present in the superalloys, such as NiO, Fe<sub>2</sub>O<sub>3</sub>, Al<sub>2</sub>O<sub>3</sub>, MoO<sub>3</sub>, and CoO. The presence of multiple oxides can lead to an acceleration of the corrosion rate because of a synergistic dissolution process, that is, some metallic oxides can undergo an acid dissolution process and others a basic dissolution process. This will promote changes in the basicity of the molten salts increasing the dissolution rate of the metallic oxides. After that, it is possible that the molten salts can be saturated with corrosion products, and the basicity stabilized at a value where the metallic oxides have approximately equal solubility. Therefore, sustained hot corrosion of the alloy does not continue (Ref 11). However, in specific cases of corrosion by molten salts that are rich in vanadium, if the Cr content in the alloy is depleted, Ni can contribute to protect the alloy due to the formation of highly stable refractive corrosion products on the alloy surface (Ni<sub>3</sub>V<sub>2</sub>O<sub>8</sub> and Ni<sub>2</sub>V<sub>2</sub>O<sub>7</sub>) (Ref 12).

Corrosion by molten salts is an electrochemical process since molten salts are excellent ionic conductors and show acid/

P.D. Silva-Leon, Facultad de Ciencias Químicas e Ingeniería, Universidad Autónoma del Estado de Morelos, Av. Universidad 1001, 62209 Cuernavaca, Morelos, Mexico; O. Sotelo-Mazon, G. Salinas-Solano, and S. Valdez, Instituto de Ciencias Físicas, Universidad Nacional Autónoma de México (UNAM), Av. Universidad s/n, 62210 Cuernavaca, Morelos, Mexico; J. Porcayo-Calderon and J.G. Gonzalez-Rodriguez, CIICAp, Universidad Autónoma del Estado de Morelos, Av. Universidad 1001, 62209 Cuernavaca, Morelos, Mexico; and L. Martinez-Gomez, Instituto de Ciencias Físicas, Universidad Nacional Autónoma de México (UNAM), Av. Universidad s/n, 62210 Cuernavaca, Morelos, Mexico; and Corrosion y Protección (CyP), Buffon 46, C.P. 11590 Mexico City, Mexico. Contact e-mail: oscarotelo.m@hotmail.com.

base behavior. Hence, the corrosion rate can be determined using electrochemical techniques (Ref 13). Cyclic corrosion tests are also important for determining the behavior of the protective oxide layer (Ref 14). A previous investigation carried out cyclic corrosion tests on different coatings of Cr<sub>3</sub>C<sub>2</sub>-NiCr, NiCrBSi, Stellite-6, or Ni-20Cr on Ni-based superalloys (Superni 75). The evaluations were made in a mixture of salts (Na<sub>2</sub>SO<sub>4</sub>-60%V<sub>2</sub>O<sub>5</sub>) at 900 °C and revealed that the Ni20Cr coating had the highest corrosion resistance. This result was attributed to the formation of oxides and spinels of Ni and Cr (Ref 15).

Thus, the goal of the present study was to evaluate the performance of Ni20Cr alloy and Inconel 600 in NaVO<sub>3</sub> at 700 °C. Another objective was to observe if the corrosion phenomena mentioned above will take place (synergistic dissolution and formation of vanadates) and how they affect the corrosion behavior of each alloy. The corrosion evaluations were taken using electrochemical techniques and cyclic corrosion tests. In addition, SEM and DRX analysis were used to support the results obtained. It is well-known that the Inconel 600 is a commercial superalloy commonly used in such systems.

## 2. Experimental Procedure

### 2.1 Testing Materials

Ni20 (wt.%) Cr alloy was made from commercial Ni20Cr powder using a quartz crucible in an induction furnace. Inconel 600 alloy was used as a reference material, which contained 16 Cr, 8 Fe, 1.5 Mn, 0.5 Si, 1.0 Cu, and 0.15 C (wt.%), which are balanced with Ni (according to the manufacturer Goodfellow). Both alloys were cut into samples measuring 8 × 5 × 6 mm. The samples were ground with 600 grade emery paper.

### 2.2 Corrosion Test

The corrosion resistance of the materials was evaluated using electrochemical techniques and cyclic corrosion tests. Electrochemical measurements were taken using conventional three-electrode electrochemical cells where either Ni20Cr or Inconel 600 was the working electrode. Platinum wire was used as the reference electrode and counter electrode. The working electrode was made by spot welding the alloy of interest (Ni20Cr or Inconel 600) to a Ni20Cr wire. To protect the wire from the corrosive environment, it was inserted in a mullite tube, and the space left between the ceramic tube and sample was sealed with refractory cement. The corrosive salt used was sodium metavanadate (NaVO<sub>3</sub>) at a temperature of 700 °C in static air. The corrosive salt was contained in an aluminum crucible and heated in a tubular electric furnace until it reached the test temperature. The arrangement of electrodes was then submerged in molten salt and stabilized for 30 min before starting the test.

Potentiodynamic polarization curves were obtained by applying polarization from -400 to 1400 mV with respect to the corrosion potential ( $E_{\text{corr}}$ ) at a scan rate of 1 mV/s. Linear polarization resistance measurements (LPR) were performed by polarizing the working electrode at ± 10 mV with respect to open-circuit potential (OCP) at a sweep rate of 10 mV/min. Electrochemical impedance spectroscopy measurements (EIS) were performed at OCP by applying a sinusoidal signal with an

amplitude of ± 10 mV in a frequency range of 10,000-0.01 Hz.

Cyclic corrosion tests were carried out by applying a corrosive salt film to the alloys. This was done by mixing NaVO<sub>3</sub> powder with distilled water to form a paste, which was added to the surface of the alloys using a brush. The samples coated with the corrosive salt were dried at room temperature and then heated to 250 °C for 2 h until a constant weight was reached. An average of 5 mg/cm<sup>2</sup> of the NaVO<sub>3</sub> was added to the surfaces of the samples. The cyclic corrosive tests were done in triplicate.

Once the alloys were coated, they were placed in aluminum crucibles and put in an electric furnace at 700 °C. The cyclic corrosive tests were done using 100 cycles, where each cycle consisted of one to 24 h. After that, data were recorded every 3 h until the end of the test. The changes in mass of the alloys were recorded using a digital balance with a sensitivity of 0.0001 g. The samples were cooled down to room temperature before recording the mass.

### 2.3 Scanning Electron Microscopy (SEM) and X-Ray Diffraction (XRD)

The corroded samples were encapsulated in epoxy resin and then ground with emery paper and polished with a 0.3-μm aluminum suspension. To avoid the dissolution of the corrosion products in water, the grinding and polishing stages were done using ethanol. The encapsulated and metallographically prepared samples were observed with a JEOL JSM-IT500 scanning electron microscope, and microchemical analysis was performed with a Bruker Flash 630 energy disperse spectrometer attached to it.

X-ray diffraction analyses were carried out using a Rigaku diffractometer with Cu K $\alpha$  radiation in order to the compounds present in the alloys. The analysis done before the corrosion test was performed on only bulk Ni20Cr alloy. However, after the corrosion test, the corrosion products were determined with powder obtained at the interface of both alloys evaluated for 100 cycles. The compounds were identified using the Match software and the PDF-2 database.

## 3. Results and Discussion

### 3.1 Potentiodynamic Polarization Curves

Figure 1 shows the potentiodynamic polarization curves for both Ni20Cr and Inconel 600 alloys evaluated in NaVO<sub>3</sub> at 700 °C in static air. The anodic branches of both materials showed active behavior toward potentials that were slightly above their corrosion potential. That is, the anodic current density increased rapidly with a small increase of potential in the noble direction (Ref 16). This behavior is a consequence of continuous dissolution of the alloy elements due to the high affinity of V for Cr and Ni (Ref 17-19).

Subsequently, both materials showed an increment in the slopes of their anodic branches. This behavior can be associated with the formation of more stable corrosion products (Ni vanadates) with better protective properties than those of Cr<sub>2</sub>O<sub>3</sub> (Ref 12). Table 1 shows the electrochemical parameters obtained from the polarization curves. In general, the two alloys showed similar behavior, but the Ni20Cr alloy showed a more noble corrosion potential and lower corrosion current

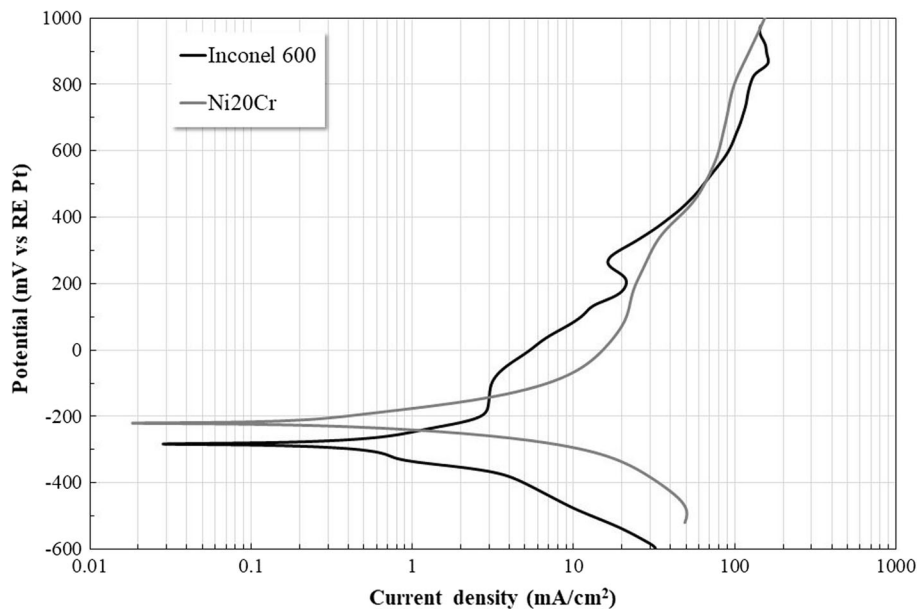


Fig. 1 Potentiodynamic polarization curves of Ni20Cr alloy and Inconel 600 in NaVO<sub>3</sub> at 700 °C in static air

Table 1 Electrochemical parameters of Ni20Cr alloy and Inconel 600

| Material    | $E_{\text{corr}}$ , mV | $I_{\text{corr}}$ , mA/cm <sup>2</sup> | Ba  | Bc  |
|-------------|------------------------|--|-----|-----|
| Ni20Cr      | -225                   | 0.447                                  | 98  | 45  |
| Inconel 600 | -286                   | 0.612                                  | 133 | 177 |

density. This suggests the formation of corrosion products (Cr<sub>2</sub>O<sub>3</sub>, NiO and Ni vanadates), with better protective characteristics than the ones formed by the Inconel 600 (Ref 20). Additionally, it has been reported that the corrosion resistance of Ni-based alloys (Inconels) is related to its chemical composition, mainly with its chromium content (Ref 21). Probably, the highest content of Cr and Ni of the Ni20Cr alloy compared with Inconel 600 promotes a faster growth of the corrosion-product layer that reduces the attack by molten salt of the alloy surface.

### 3.2 Open-Circuit Potential (OCP) Measurements

Figure 2 shows the open-circuit potential (OCP) of the Ni20Cr and Inconel 600 alloys. The Ni20Cr alloy exhibited a shift in OCP toward more active values during the first 4 h of immersion but then shifted toward slightly nobler values and reached quasi-stable behavior. This result suggests that a process of continuous dissolution of the protective oxide occurred during the first 4 h of immersion, and then more stable corrosion products tended to form (Ref 22). The passive layer could correspond to Cr oxide or corrosion products that prevent the diffusion of aggressive species into the metal surface (Ref 12-19).

The OCP for Inconel 600 showed an abrupt shift toward nobler values during the first 6 h of immersion and shifted toward more active values after 14 h. After that, it reached an apparent steady state. This behavior suggests that Inconel 600 rapidly developed a passive layer. However, this layer was not stable and was easily dissolved by the corrosive environment, which led to the formation of non-protective corrosion

products. The apparent steady state could be caused by the accumulation of corrosion products that hindered the diffusion of NaVO<sub>3</sub> into the metal surface.

Inconel 600 showed more active behavior, which was possibly due to its low content of Cr and the presence of non-protective elements Fe, Mn, and Cu. The greater content of Cr and the absence of other alloying elements in the Ni20Cr alloy promoted the development of a more stable protective layer of Cr<sub>2</sub>O<sub>3</sub> that is denser and thicker than the one that developed on Inconel 600. This resulted in a more noble potential for the Ni20Cr alloy (Ref 23).

### 3.3 Linear Polarization Resistance (LPR) Measurements

Figure 3 shows the corrosion current density ( $i_{\text{corr}}$ ) of Ni20Cr and Inconel 600 alloys in NaVO<sub>3</sub> at 700 °C. The  $i_{\text{corr}}$  values were obtained from the LPR measurements by using the Stern–Geary equation (Ref 24):

$$i_{\text{corr}} = \frac{b_a b_c}{2.3R_p(b_a + b_c)} \quad (\text{Eq 1})$$

where  $R_p$  is the polarization resistance, and  $b_a$  and  $b_c$  are the anodic and cathodic Tafel slopes, respectively (Table 1). The Ni20Cr alloy showed the lowest  $i_{\text{corr}}$  values with a constant decrease during the 12 h of immersion, but after that time, it remained steady until the end of the test. This behavior could be associated with the low reactivity of Cr in the presence of NaVO<sub>3</sub> in free corrosion conditions (Ref 19), as well as the formation of protective corrosion products with refractory characteristics due to the reaction between the Ni and vanadium salts (Ref 12).

The tendency of  $i_{\text{corr}}$  for Inconel 600 is consistent with the more active behavior observed in the OCP measurements. Inconel 600 showed the greatest corrosion current density with a decrease for the first 6 h of immersion and then a slight increase. Stable behavior occurred in the last 6 h of the test. This behavior could be associated with the low content of Cr and the presence of other elements (Fe, Mn, and Cu) that are unable to form protective oxides. The presence of multiple oxides can lead to a synergistic

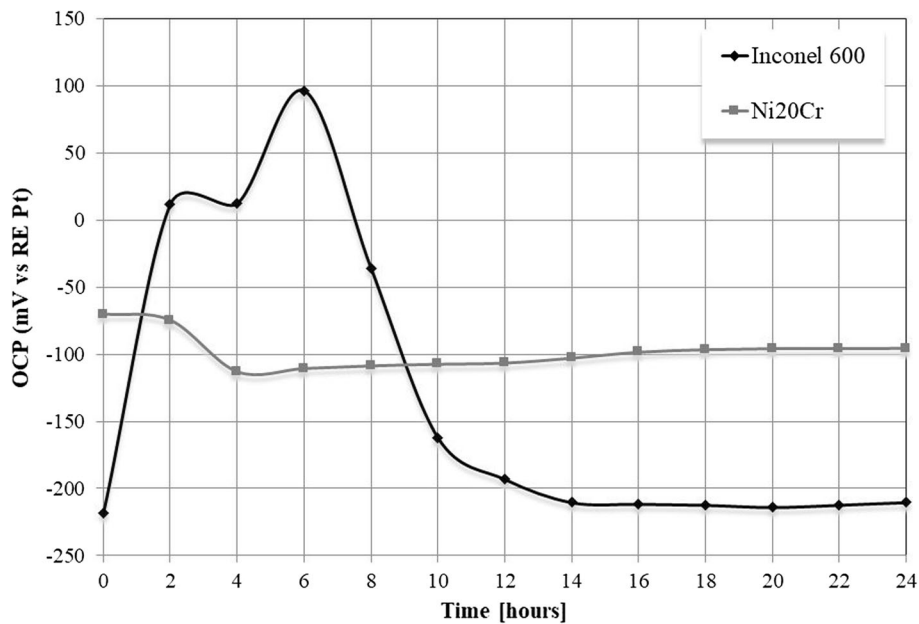


Fig. 2 Open-circuit potential of Ni20Cr alloy and Inconel 600 in NaVO<sub>3</sub> at 700 °C in static air

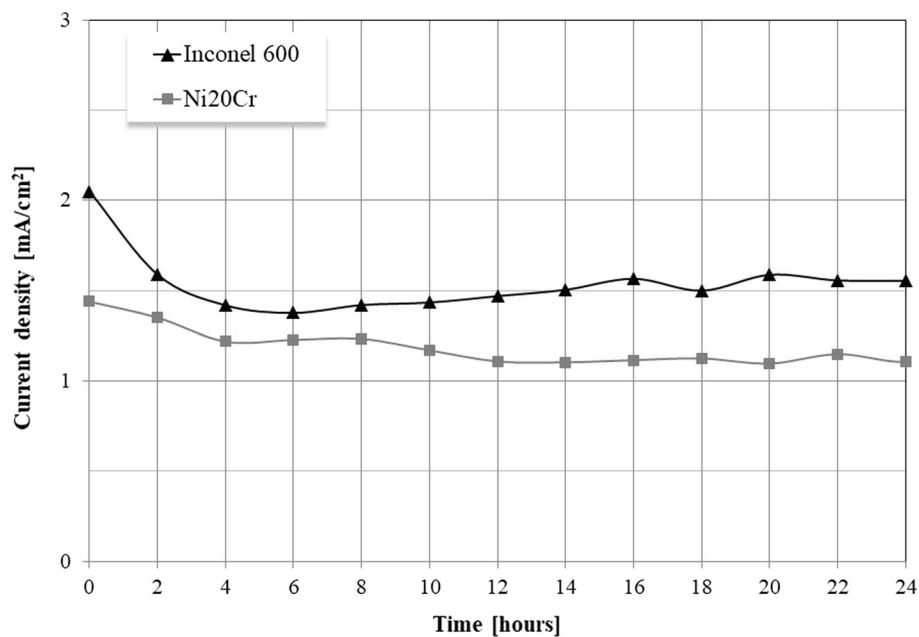


Fig. 3 Corrosion current density of Ni20Cr alloy and Inconel 600 in NaVO<sub>3</sub> at 700 °C in static air

dissolution process that decreases the corrosion resistance of the materials (Ref 6, 21, 25). The  $i_{\text{corr}}$  values observed by both alloys are similar to those reported for pure Cr in similar test conditions (Ref 3). However, the better performance of Ni20Cr alloy could be because the alloy is formed from only two elements. Cr showed the lowest reactivity in NaVO<sub>3</sub>, and the Ni formed stable and protective corrosion products.

### 3.4 Electrochemical Impedance Spectroscopy (EIS) Measurements

Figure 4 and 5 show the evolution of the impedance spectra (Nyquist and Bode format) for Ni20Cr and Inconel 600 alloys in NaVO<sub>3</sub> at 700 °C. The Nyquist diagram of the Ni20Cr alloy

(Fig. 4) showed two capacitive, depressed semicircles, one at high and intermediate frequency and a second one at low frequencies. The second capacitive semicircle increased in diameter as the immersion time increased, which indicates an increase in the corrosion resistance (Ref 26). This is consistent with the phase angle format of the Bode diagram, which showed the formation of two time constants. The first was observed around 0.1 Hz at 0 h and at higher frequencies (1-10 Hz) as time passed. The second time constant was observed at lower frequencies of 0.1 Hz with an increment in phase angle of 16°-40° over time. The formation of two time constants indicates the presence of two interfaces. The first one is associated with the interface of the corrosion products and

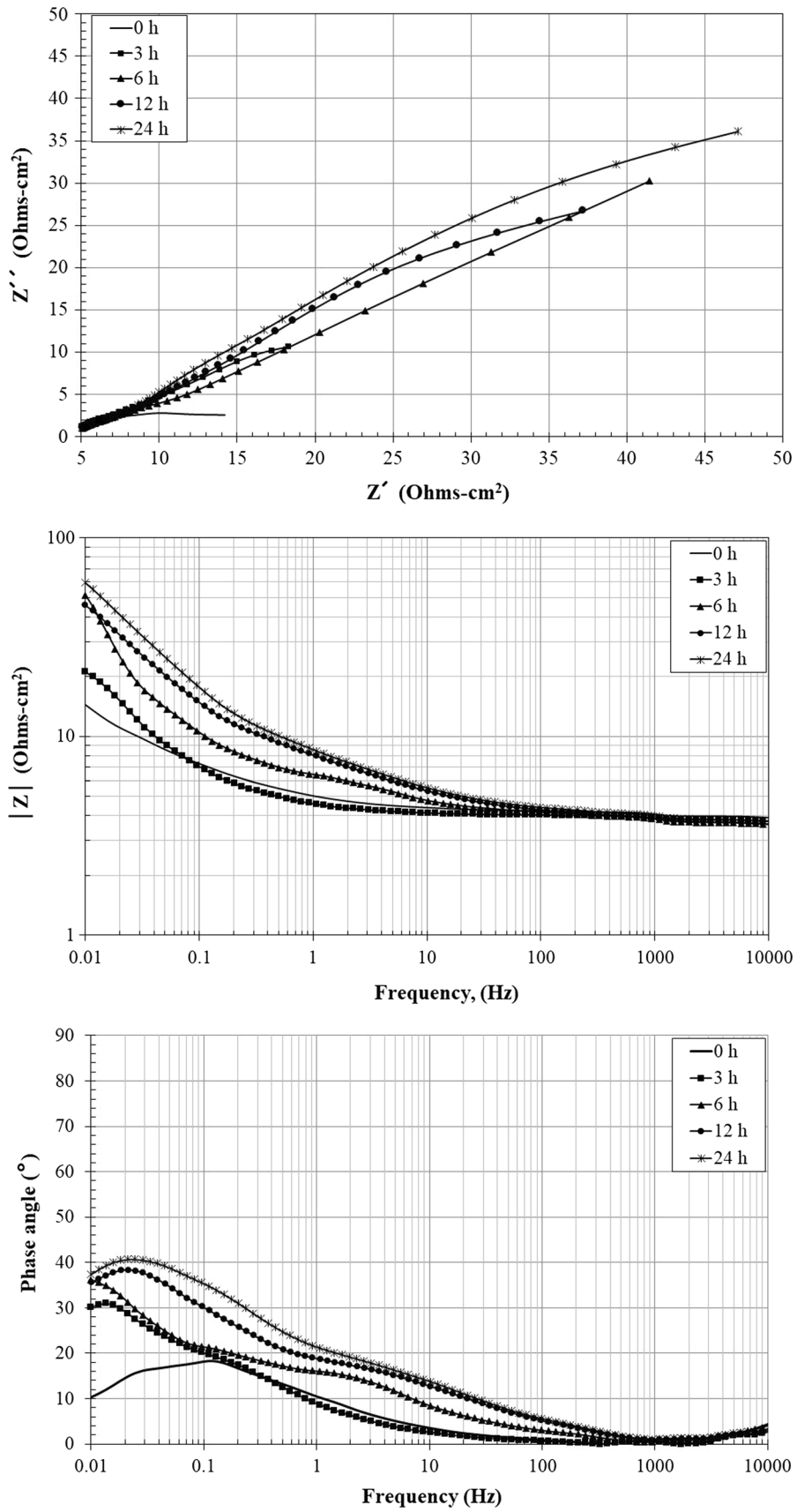


**Fig. 4** Impedance spectra of Ni20Cr alloy in  $\text{NaVO}_3$  at  $700\text{ }^\circ\text{C}$  in static air

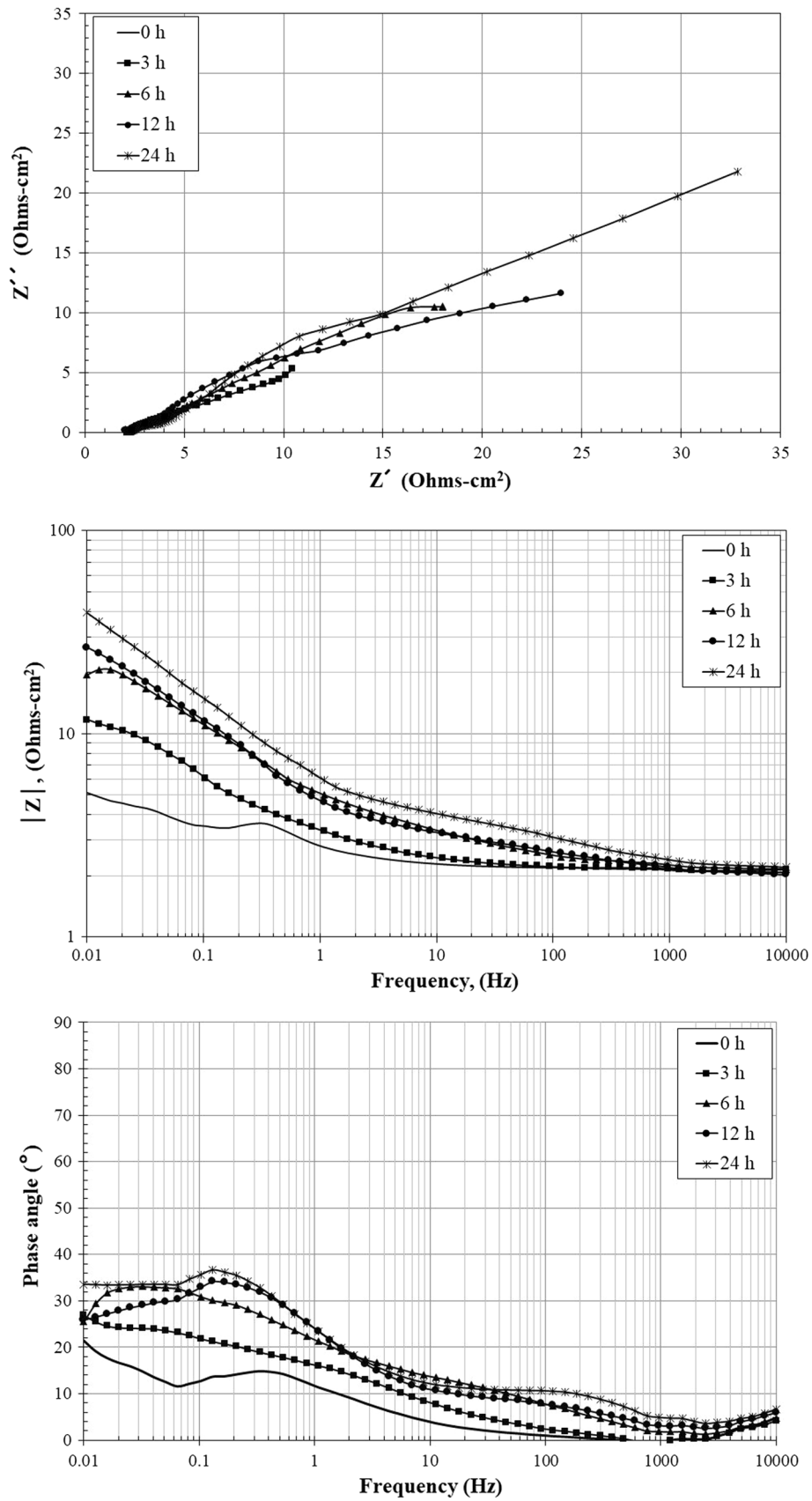


Fig. 5 Impedance spectra of Inconel 600 in  $\text{NaVO}_3$  at  $700\text{ }^\circ\text{C}$  in static air

molten salt, while the second is associated with the interface between the protective oxide and corrosion products.

In the impedance module format of the Bode diagram ( $|Z|$ ), the charge transfer resistance increased over time in the low-frequency region, which is consistent with the evolution of the second time constant and the capacitive semicircle observed in the Nyquist diagram. The absence of the low-frequency plateau indicated that the charge transfer resistance is higher than the last one obtained. This is a consequence of the formation of two protective layers on the alloy surface, which reduced the ion transport and thus the corrosion rate of the alloy (Ref 27).

Figure 5 presents the impedance spectra over time for Inconel 600, for which the behavior is similar to that of Ni20Cr alloy. The Nyquist diagram shows two capacitive semicircles, of which the diameter increased over time. The phase angle format of the Bode diagram also presented two time constants, with the first one located at 0.1-1.0 Hz at the beginning of the test, which was displaced around 200 Hz over time. The second one was observed at frequencies less than 0.1 Hz and then changed to frequencies around 0.1-0.3 Hz over time. The displacement of the time constants at higher frequencies is associated with an increment in the thickness of the layer of corrosion products (Ref 28).

Similarly, the impedance module diagram showed an increase in the charge transfer resistance, which is associated with the increase in the maximum phase angle of the second time constant. The magnitude of the maximum phase angle is associated with a more capacitive behavior of the protective oxide. Therefore, this behavior may correspond to the growth of a protective oxide or the accumulation of corrosion products, which restricted the diffusion of the corrosive agent. The impedance spectra show that Inconel 600 had poorer performance than Ni20Cr alloy, which is consistent with the electrochemical tests.

Figure 6 and 7 show the cross sections and microchemical element mapping for both alloys after 24 h of immersion in  $\text{NaVO}_3$  at 700 °C. In Ni–Cr alloys, Cr has a greater oxygen affinity than Ni. Thus, it forms a passive layer based on Cr and spinels of Ni–Cr oxides on the alloy surface (Ref 29-32). Figure 6 shows that the Ni20Cr alloy has corrosion-product scales on the surface. The element mapping indicated the high densities of Cr, V, and O. There was no evidence of a protective film of  $\text{Cr}_2\text{O}_3$ , which suggests that it was dissolved by  $\text{NaVO}_3$ , with a non-protective  $\text{CrVO}_4$  film forming according to reaction (2) (Ref 19):

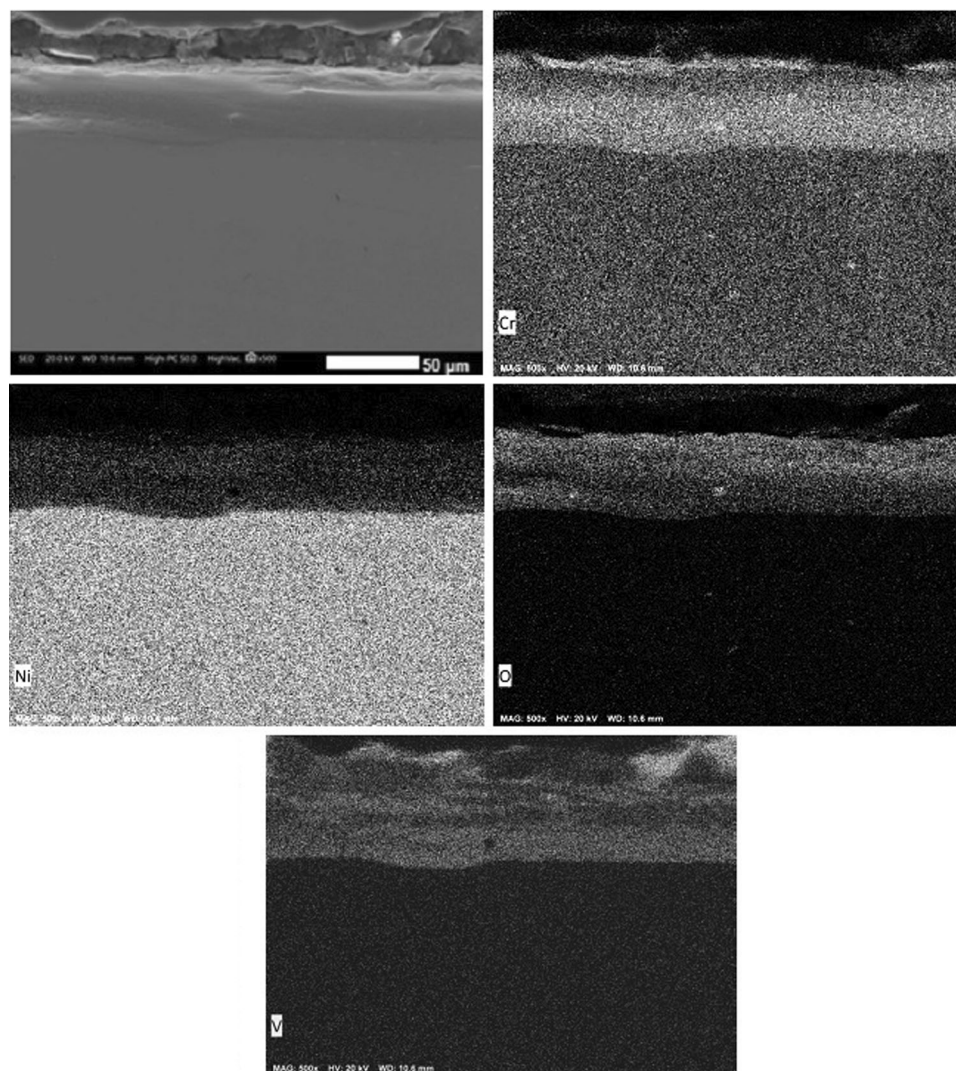
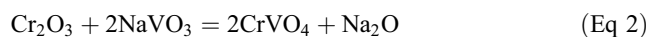


**Fig. 6** Cross sections and element mapping of Ni20Cr alloy after being exposed to  $\text{NaVO}_3$  at 700 °C for 24 h

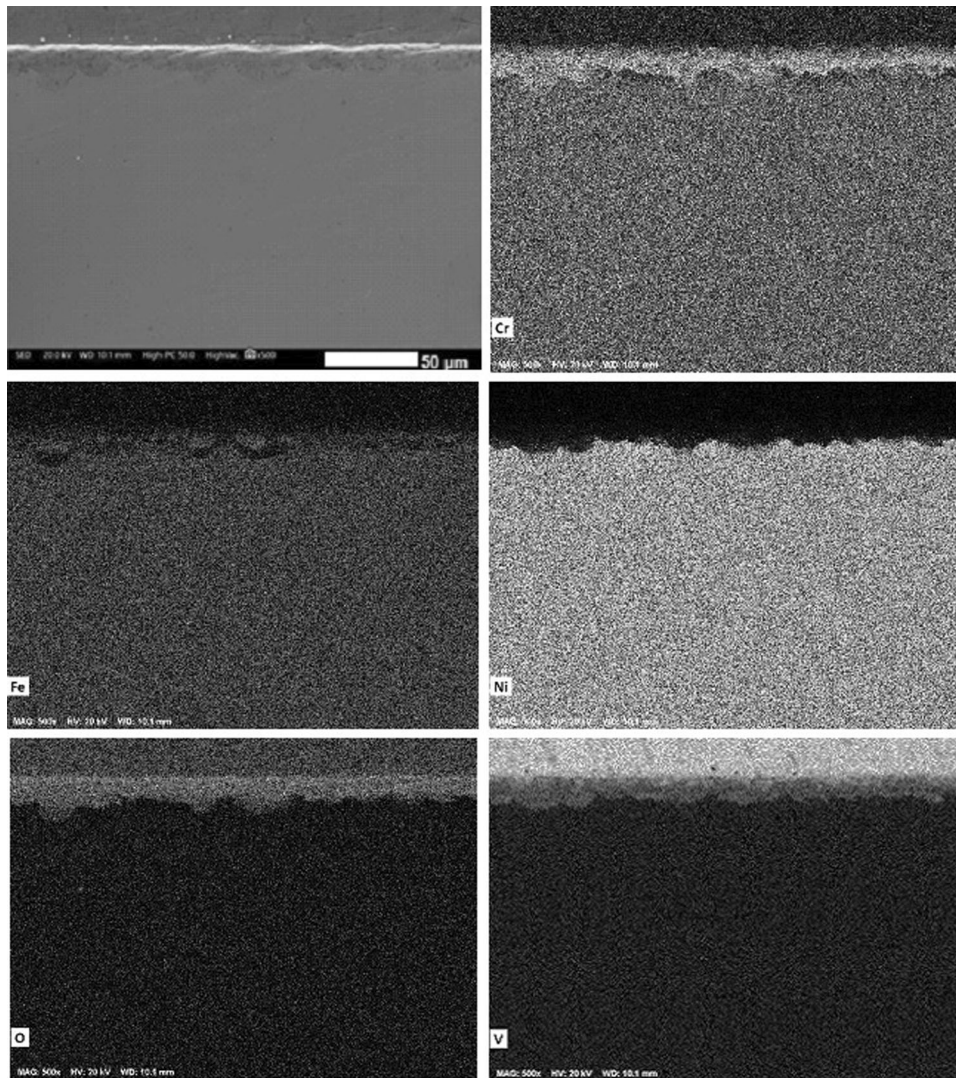
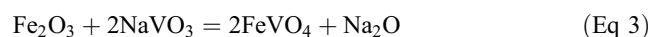


**Fig. 7** Cross sections and element mapping of the Inconel 600 after being exposed to NaVO<sub>3</sub> at 700 °C for 24 h

According to this previous reaction, the dissolution of protective oxide is associated with an increment in the basicity of the melt (Na<sub>2</sub>O), resulting in lower corrosivity (Ref 6).

The microchemical element mapping of Inconel 600 is shown in Fig. 7. There was a layer of corrosion products rich in Cr, Fe, O, and V. Once again, there was no evidence of a protective oxide based on Cr, which suggested a continuous dissolution process of the oxides that developed on the alloy surface. Another important feature is the alloy profile, which suggests that a localized corrosion process took place. This contrasts with the one observed on the Ni20Cr alloy, which presented a homogenous corrosion process according to the profile of the alloy.

In addition, there were zones that were depleted of Cr and enriched in Ni in the alloy, which suggests that the Cr content of the alloy was not able to regenerate the protective oxide layer. Thus, the corrosion of the alloy was accelerated by elements with low protection capacity, such as Fe. This suggests that the degradation of Inconel 600 occurred through the dissolution of Cr<sub>2</sub>O<sub>3</sub> (Eq 2) along with the dissolution of Fe<sub>2</sub>O<sub>3</sub> according to the following equation:



In the case of the Ni20Cr alloy, the dissolution reactions of the oxides caused an increase in basicity of the melt and decreased its corrosivity. However, due to the depletion of Cr on the surface of the alloy, less stable and less protective oxides (Fe<sub>2</sub>O<sub>3</sub>) were formed, which favored the degradation of the alloy.

### 3.5 Cyclic Corrosion Tests

Figure 8 shows the mass gain kinetics of both Ni20Cr and Inconel 600 alloys exposed to cyclic corrosion in NaVO<sub>3</sub> at 700 °C for 100 cycles in static air. The Ni20Cr alloy presented a fast mass increase during the firsts 12 cycles of the test. Then, there was a marked decrease in the mass gain rate during the rest of the test. The marked decrease in the slope of the mass gain curve of the Ni20Cr is probably due to the formation of a stable protective oxide layer or the accumulation of dense and adherent corrosion products on the metal surface, which result in a decrease in the corrosion rate (Ref 33). In contrast, Inconel 600 showed a higher mass gain with a marked increasing trend



during the entire test without visible evidence of reaching a stationary state. The higher mass increase for Inconel 600 could be related to the constant growth of a non-adherent and porous oxide layer, which allows a higher diffusion of corrosive species into the metal surface.

The kinetic parameters of the mass gains were determined by fitting the data using a parabolic rate law. This made it possible to determine the parabolic rate constant,  $kp$ . Different procedures can be used to calculate  $kp$ . One consists of relating the mass gain ( $\Delta w/A$ ) and the exposition time ( $t$ ) according to equation,  $(\frac{\Delta w}{A}) = \sqrt{kp}t^n$ . According to this equation, strictly parabolic behavior occurs when  $n = 0.5$ .

In Fig. 8, the continuous lines correspond to the fitting of the experimental data. According to the fitting, the  $n$  values for Ni20Cr and Inconel 600 alloys are 0.4053 and 0.6324, respectively. Both values showed a deviation from the parabolic model. Ni20Cr alloy had a  $kp$  value of  $0.7111 \text{ mg}^2 \text{ cm}^{-4} \text{ h}^{-1}$ , whereas that for Inconel 600 was  $1.3512 \text{ mg}^2 \text{ cm}^{-4} \text{ h}^{-1}$ . The lower value obtained for the Ni20Cr alloy indicates better performance (Ref 33).

Another way to determine  $kp$  is using a linear least square algorithm as a function in the form of  $(\frac{\Delta w}{A})^2 = kpt$  (Ref 34, 35), where  $kp$  is obtained from the slope of the line obtained by graphing  $(\Delta w/A)^2$  versus  $t$ . In this case, the model strictly agrees with the fitted parabolic when  $n = 0.5$ . The fitting of the

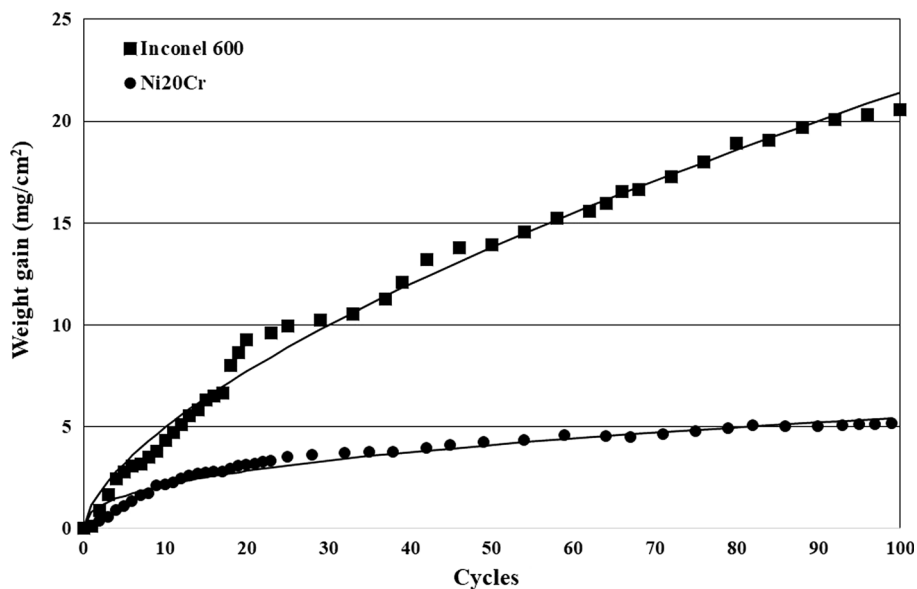


**Fig. 8** Kinetics of mass gain of Ni20Cr and Inconel 600 under a cyclic corrosion process in  $\text{NaVO}_3$  at  $700^\circ\text{C}$  and fitting of the data using a parabolic law (Eq 4)

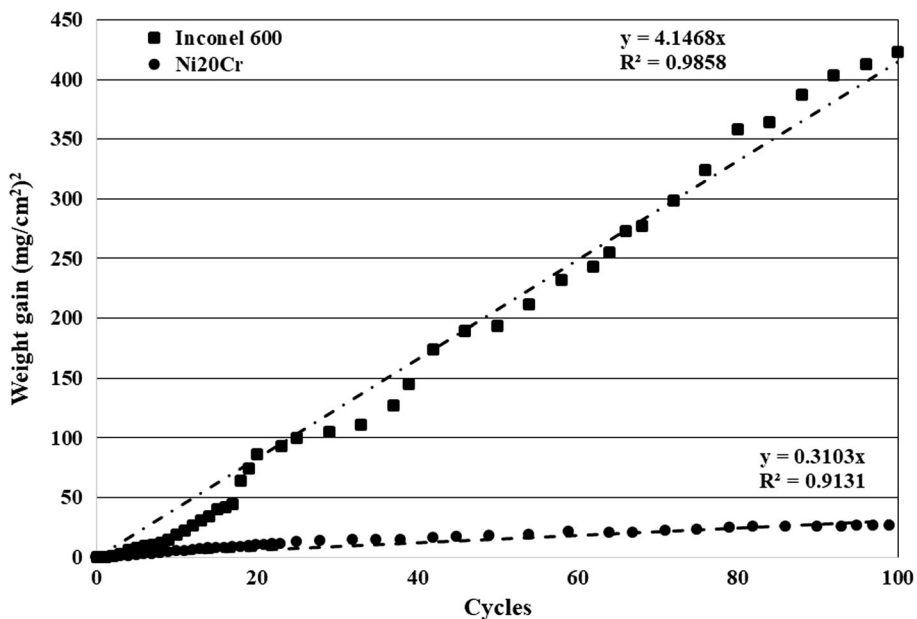


**Fig. 9** Mass gain parabolic behavior  $(\text{mg}/\text{cm}^2)^2$  vs. time for Ni20Cr alloy and Inconel 600 in  $\text{NaVO}_3$  at  $700^\circ\text{C}$  during 100 cycles

kinetic data using this model is shown in Fig. 9. The value of  $k_p$  for Ni20Cr alloy was  $0.3103 \text{ mg}^2 \text{ cm}^{-4} \text{ h}^{-1}$ , whereas that for Inconel 600 was  $4.1468 \text{ mg}^2 \text{ cm}^{-4} \text{ h}^{-1}$ . Once again, the Ni20Cr alloy showed the lowest value of  $k_p$ .

Figure 10 shows the behavior of the instant parabolic rate constant,  $k_{pi}$ , for Ni20Cr and Inconel 600 alloys according to equation,  $k_p^i = \frac{d(\frac{\Delta w}{A})^2}{dt}$  (Ref 34). The Ni20Cr alloy showed higher  $k_{pi}$  at the beginning of the test, which indicates a higher corrosion rate. However, after ten cycles, the values tended to reach a quasi-stable state with lower perturbations. This could

be due to the development of a stable protective layer on the surface, which restricted the diffusion of the corrosive species. In contrast, Inconel 600 alloy showed higher  $k_{pi}$  without a tendency to reach steady state during the entire test. The instabilities observed in the  $k_{pi}$  could be related to the formation of a non-protective oxide layer on the surface (Ref 21).

In addition, the better performance of Ni20Cr alloy could be related to its higher content of Cr than Inconel 600 (Ref 21, 36). Inconel 600 contains a significant amount of Fe (8 wt.%), which can cause the formation of the iron oxides or mixed

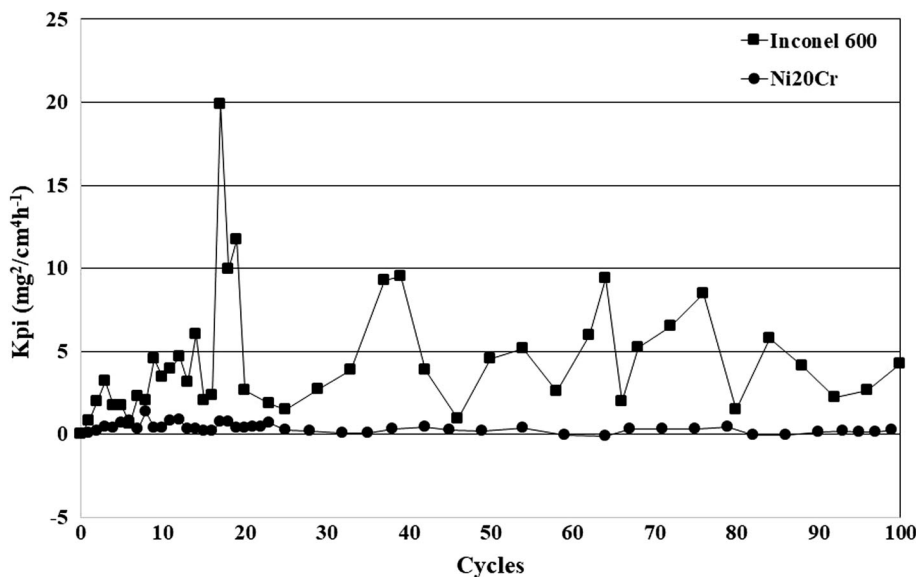


Fig. 10 Instant parabolic rate constant ( $k_{pi}$ ) of Ni20Cr alloy and Inconel 600 in  $\text{NaVO}_3$  at  $700^\circ\text{C}$  during 100 cycles

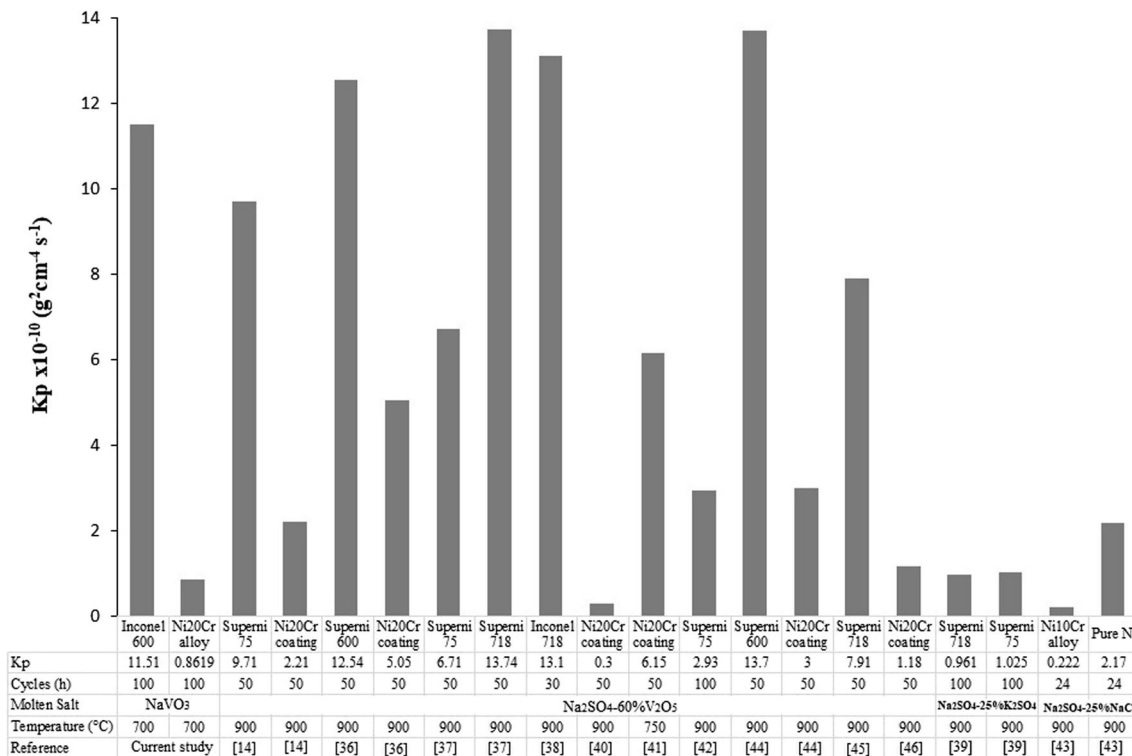
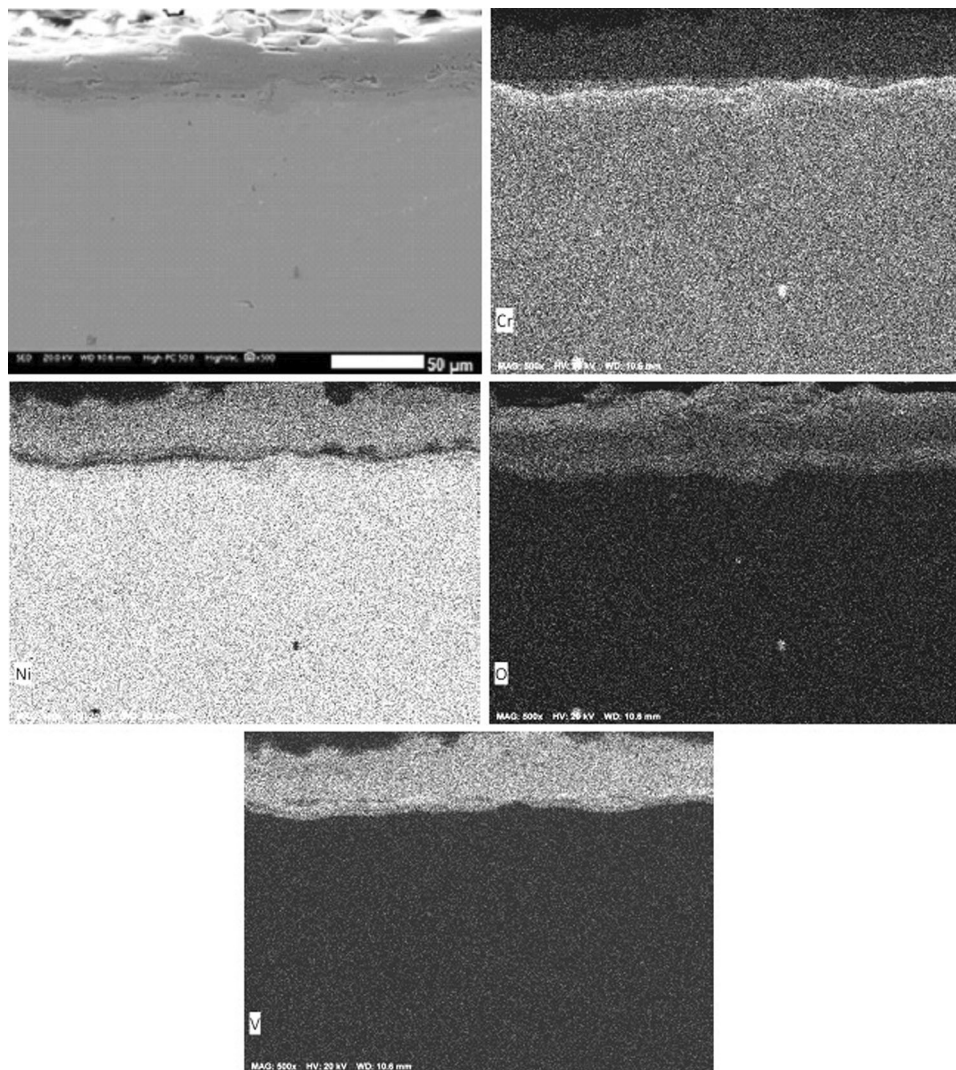


Fig. 11 Comparison between  $K_p$  of coatings and Ni-based alloys with different temperatures and molten salt environments



**Fig. 12** Cross sections and element mapping of the Ni20Cr alloy at the end of the cyclic corrosion test

oxides on the protective layer of  $\text{Cr}_2\text{O}_3$ . The formation of protective layers based on more than one metal can cause synergetic dissolution, which accelerates the corrosion process of the alloy (Ref 6, 37). In general, the Ni20Cr alloy showed an average  $k_{pi}$  of  $0.3462 \text{ mg}^2 \text{ cm}^{-4} \text{ h}^{-1}$ , whereas that for Inconel 600 was  $4.3793 \text{ mg}^2 \text{ cm}^{-4} \text{ h}^{-1}$ . This indicates that Inconel 600 has a higher mass gain during the cyclic corrosion process.

The variation of  $k_p$  with the different fitting methods indicated that both alloys did not strictly follow the parabolic oxidation law. This is caused by the molten salt, which accelerates the corrosion process of the alloy. The obtained  $k_p$  values were compared with those reported in other studies (Ref 14, 38-48) for different corrosive environments, such as mixtures of  $\text{Na}_2\text{SO}_4$ -60% $\text{V}_2\text{O}_5$ ,  $\text{Na}_2\text{SO}_4$ -25% $\text{K}_2\text{SO}_4$ , and 75% $\text{Na}_2\text{SO}_4$ -25% $\text{NaCl}$  (see Fig. 11).

The  $k_p$  values obtained for Inconel 600 in  $\text{NaVO}_3$  are within the same order of magnitude as those reported for other Ni-based super alloys, such as Superni 76, 750, 75, 718, and 600, as well as for Inconel 718 in a mixture of  $\text{Na}_2\text{SO}_4$ -60% $\text{V}_2\text{O}_5$ . The  $k_p$  values of Ni20Cr alloy in  $\text{NaVO}_3$  were higher than those for the same alloy but manufactured by a thermal spray technique and tested in  $\text{Na}_2\text{SO}_4$ -60% $\text{V}_2\text{O}_5$  at 900 °C, where

$\text{Na}_2\text{SO}_4$  and  $\text{V}_2\text{O}_5$  react to form  $\text{NaVO}_3$  (Ref 40, 49). V-containing salt mixtures at temperatures higher than 700 °C produce higher  $\text{Cr}_2\text{O}_3$  dissolution, which decreases the alloy's corrosion resistance (Ref 19). This could be the reason why the Ni20Cr alloy exhibited better corrosion resistance in the present study.

The  $k_p$  values for Inconel 600 in V-free mixtures such as  $\text{Na}_2\text{SO}_4$ -25% $\text{K}_2\text{SO}_4$  were compared, and lower results were obtained for Inconel 75 and 718 alloys. This result is related to the formation of chromate since molten  $\text{Cr}_2\text{O}_3$  in sulfates reacts with oxygen to form  $4\text{CrO}_4^{2-}$ . This prevents the dissolution of any protective oxide (Ref 41, 50). However, the  $k_p$  values for Ni20Cr and Ni10Cr alloys were very similar to each other but lower than those for pure Ni in 75% $\text{Na}_2\text{SO}_4$ -25% $\text{NaCl}$ . In addition, the hot corrosion kinetics in  $\text{NaCl}/\text{Na}_2\text{SO}_4$  mixtures showed higher mass gain than those in the  $\text{Na}_2\text{SO}_4/\text{V}_2\text{O}_5$  melts. This occurred because sulfur leads to the formation of sulfides ( $\text{CrS}_3$ ) and chlorides ( $\text{CrCl}_3$ ) in the alloy, thus preventing the formation of any protective oxide (Ref 45, 51).

Additionally, it has been reported that chromium contents lower than 10% are not enough for a continuous layer of  $\text{Cr}_2\text{O}_3$  to be formed. Thus, S or Cl can diffuse into the alloy (Ref 52).

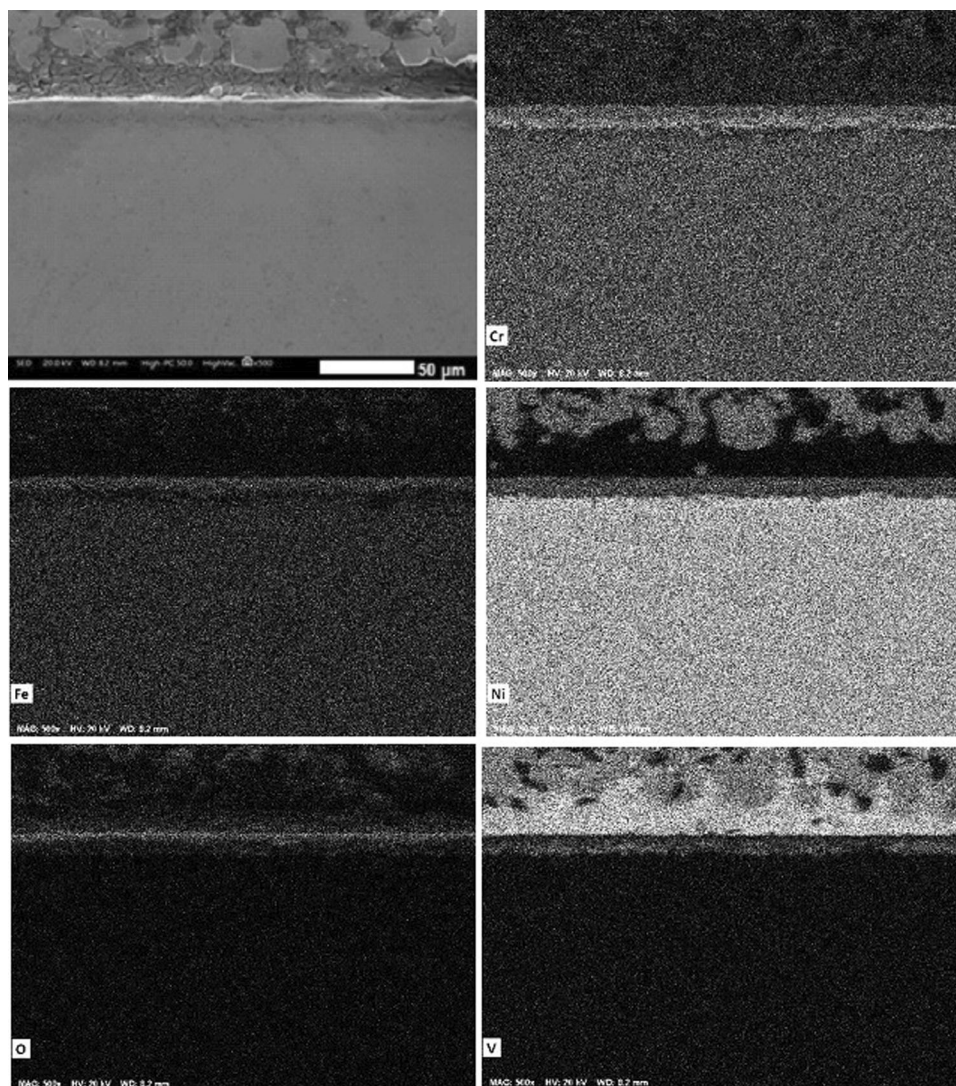
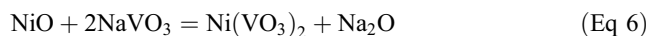
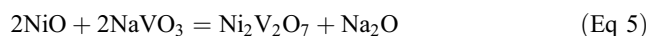
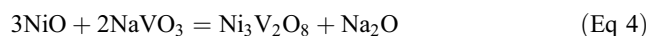


**Fig. 13** Cross sections and element mapping of the Inconel 600 at the end of the cyclic corrosion test

Therefore, in all cases,  $k_p$  for Ni20Cr alloy in  $\text{NaVO}_3$  is lower than those reported for different Ni-based alloys, regardless the type of melt, testing time, and temperature.

Figure 12 shows a micrograph of the cross sections and microchemical element mappings of the Ni20Cr alloy at the end of the cyclic corrosion test. The micrograph shows a layer that is rich in Cr and Ni oxides on its surface, above which there is corrosion-product scale that is rich in V, Ni, and Cr. The high amount of Ni in the corrosion-product layer could be caused by an initial process of metallic dissolution before a Cr-rich protective layer was established. This can be associated with the mass increase in the first 10 h of the cyclic corrosion test (Fig. 10).

The initial corrosion process of the Ni20Cr alloy favored the formation of Ni vanadates, which decrease the aggressiveness of  $\text{NaVO}_3$  and subsequently favor the development of a protective layer that is rich in Cr and Ni on the alloy. In the presence of vanadium salts, the Ni forms refractory compounds with higher melting points than 700 °C, such as  $\text{Ni}_2\text{V}_2\text{O}_7$ ,  $\text{Ni}_3\text{V}_2\text{O}_8$ , and  $\text{Ni}(\text{VO}_3)_2$  according to the following reactions (Ref 12):



Similarly, Fig. 13 shows a cross-sectional micrograph together with the microchemical element mapping of Inconel 600 at the end of the cyclic corrosion test. The surface has oxide scale that is rich Cr, Ni, and Fe, as well as V oxide. This indicated low protective capacity due to the presence of multiple metallic oxides, which favored a synergistic dissolution process that promoted the corrosion process of the alloy (Ref 6, 37). Corrosion-product scale that is rich in V, Cr, Ni, and Fe was observed on the oxide layer. It was also observed that phases rich in V and Ni (vanadates of Ni) were not able to form a protective layer on the alloy. Due to the continuous metallic dissolution process, a depletion of Cr and Fe and enrichment of Ni were observed on the alloy. These characteristics have been observed in the corrosion process in molten

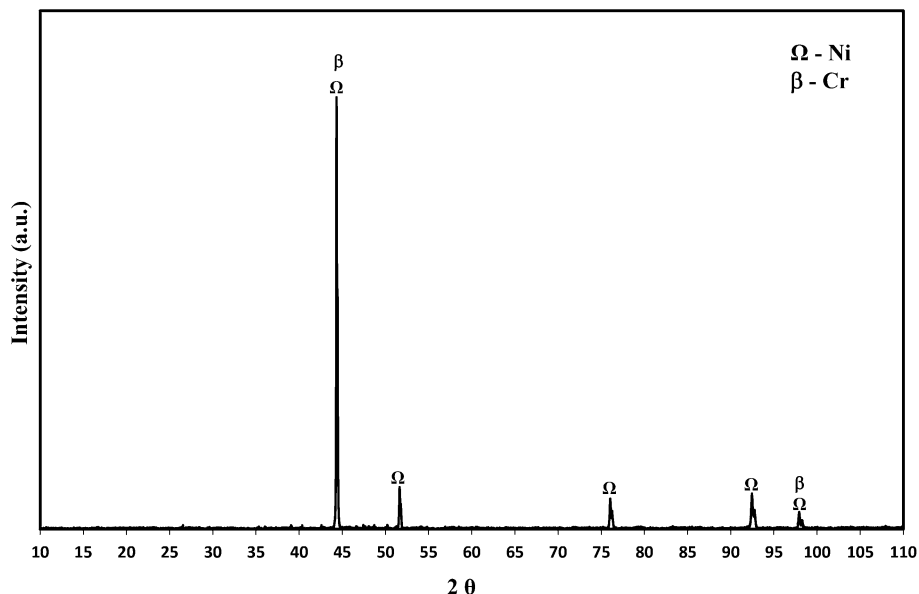


Fig. 14 XRD pattern of the Ni20Cr alloy

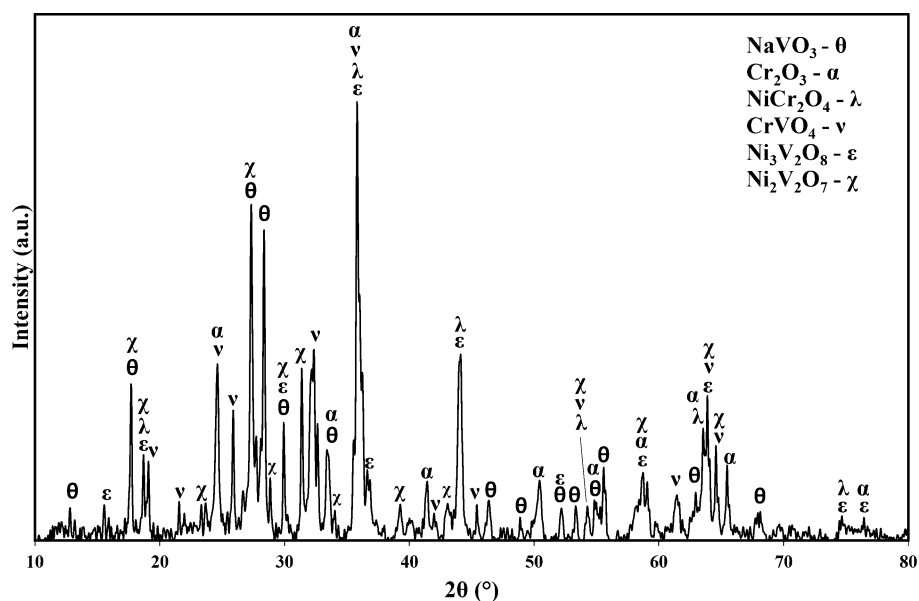


Fig. 15 XRD pattern of the corrosion products obtained from the interface of Ni20Cr alloy coated with NaVO<sub>3</sub> salt at 700 °C for 100 cycles

salt, where the alloy is not capable of developing a protective oxide (Ref 21, 53-56).

### 3.6 X-ray Diffraction Analysis

Figure 14 shows the X-ray diffraction pattern (XRD) of the as-received Ni-20Cr alloy. The highest peak can be observed at  $2\theta = 44.26^\circ$ , which is in agreement with the results reported in another works. This result indicates that there might be a superposition of two peaks that correspond to Ni (1 1 1) ( $2\theta = 44.505^\circ$  according to ICDS, Inorganic Crystal Structure Database) and Cr (1 1 0) ( $2\theta = 44.390^\circ$ ). This suggests the formation of a solid solution of Cr in Ni. The amount of Cr in Ni also increased the crystal lattice parameters, as reported

previously (Ref 57). In addition, it has been reported that  $\gamma$ -NiCr is the main phase found in Ni-Cr alloys (Ref 58).

Figure 15 shows the XRD patterns of the corrosion products for Ni20Cr after the corrosion tests in molten NaVO<sub>3</sub> at 700 °C for 100 cycles. A Cr<sub>2</sub>O<sub>3</sub> layer as well as Ni and Cr (NiCr<sub>2</sub>O<sub>4</sub>) spinel were found. Additionally, Cr (CrVO<sub>4</sub>) and Ni (Ni<sub>3</sub>V<sub>2</sub>O<sub>8</sub>, Ni<sub>2</sub>V<sub>2</sub>O<sub>7</sub>) vanadates were also identified, which reduced the corrosion rate due to the formation of Ni refractory vanadates. XRD patterns for the corrosion-product layer that formed on top of Inconel 600 showed the presence of Cr<sub>2</sub>O<sub>3</sub>, Fe<sub>2</sub>O<sub>3</sub>, Ni, and Cr spinels, and vanadates of Fe and Ni (see Fig. 16). The corrosion products identified for both alloys have been observed in other studies

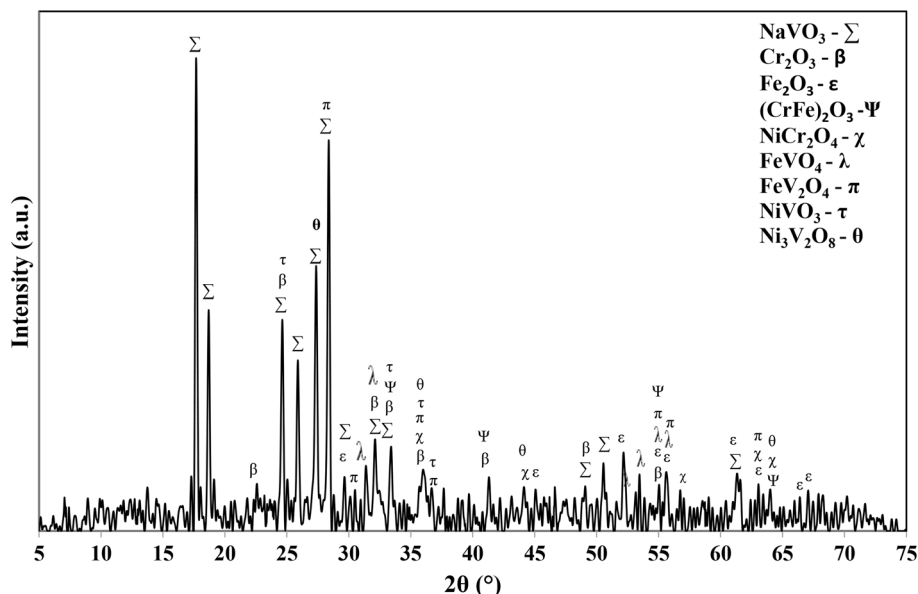


**Fig. 16** XRD pattern of the corrosion products obtained from the interface of Inconel 600 coated with  $\text{NaVO}_3$  salt at  $700^\circ\text{C}$  for 100 cycles

that evaluated Ni-based alloys in molten salts with the addition of vanadium (Ref 48, 59, 60).

#### 4. Conclusion

Ni20Cr alloy had better electrochemical and mass gain performance than Inconel 600 in  $\text{NaVO}_3$  at  $700^\circ\text{C}$ . Electrochemical tests such as LPR and EIS showed that Ni20Cr alloy had lower corrosion current density and higher charge transfer resistance than Inconel 600 alloy. This indicates better corrosion resistance due to the formation of a protective Cr oxide layer, which has better protective characteristics than the ones that formed on Inconel 600. In addition, the contents of different elements (Cr, Fe, Ni, Cu, and Mn) in Inconel 600 helped to accelerate the corrosion process. Protective layers based on different oxides lead to a synergetic dissolution process that accelerates the corrosion process.

The cyclic corrosion tests showed that Ni20Cr alloy had a lower parabolic rate constant and thus a higher corrosion resistance than Inconel 600. SEM and XRD analyses showed that a protective layer of Ni vanadates was formed on the surface of Ni20Cr alloy. These refractory compounds protected the alloy by preventing the diffusion of corrosive species.

#### Acknowledgments

O. Sotelo-Mazon is thankful to the postdoctoral fellowship DGAPA-UNAM. Jose Juan Ramos Hernandez is thanked for the support in the electron microscopy analysis.

#### References

1. N. Otsuka, *Shreir's Corrosion-Volume 1: Basic Concepts, High Temperature Corrosion, Fireside Corrosion*, 4th ed., Academic Press, New York, 2010, p 457–481

2. I.B. Singh, Corrosion and Sulphate Ion Reduction Studies on Ni and Pt Surfaces in With and Without  $\text{V}_2\text{O}_5$  in (Li, Na, K) $_2\text{SO}_4$  Melt, *Corr. Sci.*, 2003, **45**, p 2285–2292
3. O. Sotelo, C. Cuevas, J. Porcayo, V.M. Salinas, and G. Izquierdo, Corrosion Behavior of Pure Cr, Ni, and Fe Exposed to Molten Salts at High Temperature, *Adv. Mater. Sci. Eng.*, 2014, <https://doi.org/10.1155/2014/923271>
4. R.A. Mahesh, R. Jayaganthan, and S. Prakash, Evaluation of Hot Corrosion Behaviour of HVOF Sprayed Ni–5Al and NiCrAl Coatings in Coal Fired Boiler Environment, *Surf. Eng.*, 2010, **26**(6), p 413–421
5. X. Montero and M.C. Galetz, Inhibitors and Coatings Against Vanadate-Containing Oil Ash Corrosion of Boilers, *Surf. Coat. Technol.*, 2016, **304**, p 211–221
6. R.A. Rapp, Hot Corrosion of Materials: A Fluxing Mechanism?, *Corr. Sci.*, 2002, **44**, p 209–221
7. S. Bose, *High Temperature Coatings, Chap. 6-Oxidation and Corrosion Resistance Coatings*, 2nd ed., Elsevier, New York, 2018, p 97–198, <https://doi.org/10.1016/B978-0-12-804622-7.00005-X>
8. T.S. Sidhu, S. Prakash, and R.D. Agrawal, Hot Corrosion and Performance of Nickel-Based Coatings, *Corr. Sci.*, 2006, **90**(1), p 41–47
9. F. Weng, H. Yu, C. Chen, and K. Wan, Influence of Nb and Y on Hot Corrosion Behavior of Ni–Cr-based Superalloys, *Mater. Manuf. Processes*, 2015, **30**, p 677–684
10. J. Stringer, High-Temperature Corrosion of Superalloys, *Mater. Sci. Technol.*, 1987, **3**(7), p 482–493
11. Y. Longa, Y.S. Zhang, M. Takemoto, and R.A. Rapp, Hot Corrosion of Nickel-Chromium and Nickel-Chromium-Aluminum Thermal-Spray Coatings by Sodium Sulfate-Sodium Metavanadate Salt, *Corrosion*, 1996, **52**(9), p 680–689
12. J. Porcayo, J.J. Ramos, J. Mayen, E. Porcayo, G.K. Pedraza, J.G. Gonzalez, and L. Martinez, High Temperature Corrosion of Nickel in  $\text{NaVO}_3\text{-V}_2\text{O}_5$  Melts, *Adv. Mater. Sci. Eng.*, 2017, <https://doi.org/10.1155/2017/8929873>
13. C.L. Zeng and J. Li, Electrochemical Impedance Studies of Molten (0.9Na, 0.1 K) $_2\text{SO}_4$ -Induced Hot Corrosion of the Ni-Based Superalloy M38G at  $900^\circ\text{C}$  in Air, *Electrochim. Acta*, 2005, **50**, p 5533–5538
14. D. Deb, S.R. Iyer, and V.M. Radhakrishnan, A Comparative Study of Oxidation and Hot Corrosion of a Cast Nickel Base Superalloy in Different Corrosive Environments, *Mater. Lett.*, 1996, **29**(1–3), p 19–23
15. T.S. Sidhu, S. Prakash, and R.D. Agrawal, Evaluation of Hot Corrosion Resistance of HVOF Coatings on a Ni-Based Superalloy in Molten Salt Environment, *Mater. Sci. Eng. A*, 2006, **430**, p 64–78

16. E.M. Zahrani and A.M. Alfantazi, Molten Salt Induced Corrosion of Inconel 625 Superalloy in  $\text{PbSO}_4\text{-Pb}_3\text{O}_4\text{-PbCl}_2\text{-Fe}_2\text{O}_3\text{-ZnO}$  Environment, *Corr. Sci.*, 2012, **65**, p 340–359
17. N.S. Flores and C. Cuevas, High-Temperature Corrosion Investigation of the Inconel-600 in Molten Sulfate/Vanadate Mixtures Using Electrochemical Techniques, *Int. J. Electrochem. Sci.*, 2017, **12**, p 9882–9895
18. P.S. Sidky and M.G. Hocking, The Hot Corrosion of Ni-Based Ternary Alloys and Superalloys for Application in Gas Turbines Employing Residual Fuels, *Corr. Sci.*, 1987, **27**(5), p 499–530
19. J. Porcayo, V.M. Salinas, R.A. Rodriguez, and L. Martinez, Effect of the  $\text{NaVO}_3\text{-V}_2\text{O}_5$  Ratio on the High Temperature Corrosion of Chromium, *Int. J. Electrochem. Sci.*, 2015, **10**(5), p 4928–4945
20. C. Cuevas, J. Uruchurtu, J. González, G. Izquierdo, J. Porcayo, and U. Cano, Corrosion Evaluation of Alloy 800 in Sulfate/Vanadate Molten Salts, *Corrosion*, 2004, **6**(6), p 549–560
21. O. Sotelo, J. Porcayo, C. Cuevas, G. Salinas, J.J. Ramos, E. Vazquez, and L. Martinez, Corrosion Performance of Ni-Based Alloys in Sodium Metavanadate, *Int. J. Electrochem. Sci.*, 2016, **11**, p 1868–1882
22. I. Gurrappa and D.V. Reddy, Characterisation of Titanium Alloy, IMI-834 for Corrosion Resistance Under Different Environmental Conditions, *J. Alloys Compd.*, 2005, **390**(1–2), p 270–274
23. A. Nishikata and S. Haruyama, Electrochemical Monitoring of the Corrosion of Ni, Fe, and Their Alloys in Molten Salts, *Corrosion*, 1986, **42**(10), p 578–584
24. M. Stern and A.L. Geary, Electrochemical Polarization, *J. Electrochem. Soc.*, 1957, **104**(9), p 56–63
25. K.J.L. Iyer, S.R. Iyer, and V.M. Radhakrishnan, Some Aspects of Hot Corrosion of Superni by Vanadium, *Can. Metall. Q.*, 1987, **26**(1), p 53–59
26. C.H. Lin and J.G. Duh, Electrochemical Impedance Spectroscopy (EIS) Study on Corrosion Performance of CrAlSiN Coated Steels in 3.5 wt% NaCl Solution, *Surf. Coat. Technol.*, 2009, **204**(6–7), p 784–787
27. C.L. Zeng, W. Wang, and W.T. Wu, Electrochemical Impedance Models for Molten Salt Corrosion, *Corr. Sci.*, 2001, **43**(4), p 787–801
28. O. Sotelo, J. Porcayo, C. Cuevas, J.J. Ramos, J.A. Ascencio, and L. Martinez, EIS Evaluation of Fe, Cr, and Ni in  $\text{NaVO}_3$  at 700°C, *J. Spectrosc.*, 2014, <https://doi.org/10.1155/2014/949168>
29. T.S. Sidhu, S. Prakash, and R.D. Agrawal, Hot Corrosion Performance of a NiCr Coated Ni-Based Alloy, *Scr. Mater.*, 2006, **55**(2), p 179–182
30. S.P. Jeng, P.H. Holloway, and C.D. Batch, Surface Passivation of Ni/Cr Alloy at Room Temperature, *Surf. Sci.*, 1990, **227**(3), p 278–290
31. H. Ruiz, J. Porcayo, J.E. Garcia, J.M. Alvarado, L. Martinez, L.G. Trapaga, and J. Muñoz, Electrochemical Corrosion of HVOF-Sprayed NiCoCrAlY Coatings in  $\text{CO}_2$ -Saturated Brine, *J. Therm. Spray Technol.*, 2016, **25**(7), p 1330–1343
32. H. Ruiz, J. Porcayo, J.M. Alvarado, A.G. Mora, L. Martinez, L.G. Trápaga, and J. Muñoz, Influence of Oxidation Treatments and Surface Finish on the Electrochemical Behavior of HVOF Ni-20Cr Coatings, *J. Mater. Eng. Perform.*, 2017, <https://doi.org/10.1007/s11665-017-3048-1>
33. N. Jegadeeswaran, M.R. Ramesh, and K.U. Bhat, Combating Corrosion Degradation of Turbine Materials Using HVOF Sprayed 25% ( $\text{Cr}_3\text{C}_2\text{-25(Ni20Cr)}$ ) + NiCrAlY Coating, *Int. J. Corr.*, 2013, <https://doi.org/10.1155/2013/824659>
34. N. Babu, R. Balasubramaniam, and A. Ghosh, High-Temperature Oxidation of  $\text{Fe}_3\text{Al}$ -Based Iron Aluminides in Oxygen, *Corr. Sci.*, 2001, **43**(12), p 2239–2254
35. N.K. Mishra, A.K. Rai, S.B. Mishra, and R. Kumar, Hot Corrosion Behaviour of Detonation Gun Sprayed Stellite-6 and Stellite-21 Coating on Boiler Steel SAE 431 at 900 C, *J. Corr. Int.*, 2014, <https://doi.org/10.1155/2014/146391>
36. N. Bala, H. Singh, and S. Prakash, High-Temperature Oxidation Studies of Cold Sprayed Ni–20Cr and Ni–50Cr Coatings on SAE 213-T22 Boiler Steel, *Appl. Surf. Sci.*, 2009, **255**, p 6862–6869
37. Y.S. Hwang and R.A. Rapp, Synergistic dissolution of oxides in molten sodium sulfate, *J. Electrochem. Soc.*, 1990, **137**(4), p 1276–1280
38. H. Singh, S. Prakash, D. Puri, and D.M. Phase, Cyclic Oxidation Behavior of Some Plasma-Sprayed Coatings in  $\text{Na}_2\text{SO}_4\text{-60%V}_2\text{O}_5$  Environment, *J. Mater. Eng. Perform.*, 2006, **15**(6), p 729–741
39. T.S. Sidhu, S. Prakash, and R.D. Agrawal, Characterisations of HVOF Sprayed NiCrBSi Coatings on Ni- and Fe-Based Superalloys and Evaluation of Cyclic Oxidation Behaviour of some Ni-Based Super-alloys in Molten Salt Environment, *Thin Solid Films*, 2006, **515**(1), p 95–105
40. S. Saladi, J.V. Menghani, and S. Prakash, Characterization and Evaluation of Cyclic Hot Corrosion Resistance of Detonation-Gun Sprayed Ni-5Al Coatings on Inconel-718, *J. Therm. Spray Technol.*, 2015, **24**(5), p 778–788
41. S. Kamal, R. Jayaganthan, and S. Prakash, Evaluation of Cyclic Hot Corrosion Behaviour of Detonation Gun Sprayed  $\text{Cr}_3\text{C}_2\text{-25%NiCr}$  Coatings on Nickel- and Iron-Based Superalloys, *Surf. Coat. Technol.*, 2009, **203**(8), p 1004–1013
42. G. Kaushal, H. Singh, and S. Prakash, High Temperature Corrosion Behaviour of HVOF-Sprayed Ni-20Cr Coating on Boiler Steel in Molten Salt Environment at 900°C, *Int. J. Surf. Sci. Eng.*, 2011, **5**(5–6), p 415–433
43. S.S. Chatha, H.S. Sidhu, and B.S. Sidhu, High Temperature Hot Corrosion Behaviour of NiCr and  $\text{Cr}_3\text{C}_2\text{-NiCr}$  Coatings on T91 Boiler Steel in an Aggressive Environment at 750°C, *Surf. Coat. Technol.*, 2012, **206**(19–20), p 3839–3850
44. S. Kamal, R. Jayaganthan, S. Prakash, and S. Kumar, Hot Corrosion Behavior of Detonation Gun Sprayed  $\text{Cr}_3\text{C}_2\text{-NiCr}$  Coatings on Ni and Fe-Based Superalloys in  $\text{Na}_2\text{SO}_4\text{-60%V}_2\text{O}_5$  Environment at 900°C, *J. Alloys Compd.*, 2008, **463**(1–2), p 358–372
45. F. Guangyan, Q. Zeyan, C. Jingyu, L. Qun, and S. Yong, Hot Corrosion Behavior of Ni-Base Alloys Coated with Salt Film of 75% $\text{Na}_2\text{SO}_4$  + 25%NaCl at 900°C, *Rare Met. Mater. Eng.*, 2015, **44**(5), p 1112–1115
46. T.S. Sidhu, S. Prakash, and R.D. Agrawal, Hot Corrosion Studies of HVOF Sprayed  $\text{Cr}_3\text{C}_2\text{-NiCr}$  and Ni–20Cr Coatings on Nickel-Based Superalloy at 900°C, *Surf. Coat. Technol.*, 2006, **201**(3–4), p 792–800
47. A. Rahmana, V. Chawla, R. Jayaganthana, R. Chandra, and R. Ambardar, Study of Cyclic Hot Corrosion of Nanostructured Cr/Co–Al Coatings on Superalloy, *Mater. Chem. Phys.*, 2011, **126**(1–2), p 253–261
48. T.S. Sidhu, S. Prakash, and R.D. Agrawal, Performance of High-Velocity Oxyfuel-Sprayed Coatings on an Fe-Based Superalloy in  $\text{Na}_2\text{SO}_4\text{-60%V}_2\text{O}_5$  Environment at 900°C Part II: Hot Corrosion Behavior of the Coatings, *J. Mater. Eng. Perform.*, 2006, **15**(1), p 130–138
49. R.A. Mahesh, R. Jayaganthan, and S. Prakash, A Study on Hot Corrosion Behaviour of Ni–5Al Coatings on Ni- and Fe-Based Superalloys in an Aggressive Environment at 900°C, *J. Alloys Compd.*, 2008, **460**(1–2), p 220–231
50. F. Wang, X. Tian, Q. Li, L. Li, and X. Peng, Oxidation and Hot Corrosion Behavior of Sputtered Nanocrystalline Coating of Superalloy K52, *Thin Solid Films*, 2008, **516**(16), p 5740–5747
51. N. Arivazhagan, S. Narayanan, S. Singh, S. Prakash, and G.M. Reddy, High Temperature Corrosion Studies on Friction Welded Low Alloy Steel and Stainless Steel in Air and Molten Salt Environment at 650°C, *Mater. Des.*, 2012, **34**, p 459–468
52. J. Porcayo-Calderon, J.G. Gonzalez-Rodriguez, and L. Martinez, Protection of Carbon Steel against Hot Corrosion Using Thermal Spray Si- and Cr-Base Coatings, *J. Mater. Eng. Perform.*, 1998, **7**(1), p 79–87
53. A. Luna, J. Porcayo, G. Salinas, C.D. Arrieta, V.M. Salinas, and L. Martinez, Electrochemical Performance of Fe-Al Intermetallic alloys with Addition of Li, Ni and Ce in  $\text{NaVO}_3$  at 700 C, *Int. J. Electrochem. Sci.*, 2013, **8**(4), p 4641–4653
54. G. Salinas, J.G. Gonzalez, J. Porcayo, V.M. Salinas, G. Lara, and A. Martinez, Electrochemical Study on Effect of Au, Ag, Pd and Pt on Corrosion Behaviour of  $\text{Fe}_3\text{Al}$  in Molten NaCl–KCl, *Corros. Eng. Sci. Technol.*, 2014, **49**(5), p 378–385
55. G. Salinas, J. Porcayo, J.G. Gonzalez, V.M. Salinas, J.A. Ascencio, and L. Martinez, High Temperature Corrosion of Inconel 600 in NaCl-KCl Molten Salts, *Adv Mater. Sci Eng*, 2014, <https://doi.org/10.1155/2014/696081>
56. L. Romo, J.G. Gonzalez, J. Porcayo, R. Guardian, and V.M. Salinas, Study on the Effect of Co, Cr and Ti on the Corrosion of Fe40Al Intermetallic in Molten NaCl-KCl Mixture, *Intermetallics*, 2015, **67**, p 156–165
57. V. Petley, S. Sathishkumar, K.H.T. Raman, G.M. Rao, and U. Chandrasekhar, Microstructural and Mechanical Characteristics of Ni–Cr thin Films, *Mater. Res. Bull.*, 2015, **66**, p 59–64
58. D. Lou, C. He, S. Shang, C. Liu, and Q. Cai, Microstructure and Performances of Graphite Scattered  $\text{Cr}_3\text{C}_2\text{-NiCr}$  Composites Prepared by Laser Processing, *Mater. Lett.*, 2013, **93**, p 304–307

59. V. Mannava, A. Sambasiva Rao, M. Kamaraj, and R. Sankar Kottada, Influence of Two Different Salt Mixture Combinations of Na<sub>2</sub>SO<sub>4</sub>-NaCl-NaVO<sub>3</sub> on Hot Corrosion Behavior of Ni-Base Superalloy Nimonic 263 at 800°C, *J. Mater. Eng. Perform.*, 2019, **28**(2), p 1077–1093
60. D. Pradhan, G.S. Mahobia, K. Chattopadhyay, and V. Singh, Severe Hot Corrosion of the Superalloy IN718 in Mixed Salts of Na<sub>2</sub>SO<sub>4</sub> and V<sub>2</sub>O<sub>5</sub> at 700°C, *J. Mater. Eng. Perform.*, 2018, **27**(8), p 4235–4243

**Publisher's Note** Springer Nature remains neutral with regard to jurisdictional claims in published maps and institutional affiliations.